Scientia Iranica, Vol. 13, No. 3, pp 316–325

SCIENTIA IRANICA

Research Note

Simulation of Interdendritic Liquid Permeability for Low and High Solid Fractions During Solidification of Mushy Alloys

S.M.H. Mirbagheri[1]

A numerical model has been developed for the determination of liquid flow permeability through columnar dendrite during growth and segregation in Al-Si alloys. Therefore, in the present work, two separate computational models of grain growth and interdendritic liquid flow are coupled for modeling of the permeability in partly solid alloy. Grain growth is simulated, using a Cellular Automation Finite Difference (CAFD) for a 2D dendrite and fluid flow by using a Computational Fluid Dynamic (CFD) model for determining permeability. A new model has been presented for calculation and modification of dendrite permeability in high solid fractions. Simulation results show which Si concentration variations, at each time step, could transform the dendrite shape. Also, dendrite morphology could alert the interdendritic permeability factor.

INTRODUCTION

Casting engineers continually deal with macrosegregation, but, despite their efforts, segregation sometimes persists and can even reach unacceptable levels leading to expensive scrap. In addition, macrosegregation in ingots or casting parts can be an overriding factor in limiting the size and production rate of the cast product. Convection of interdendritic liquid through the dendritic mushy zone in solidifying alloys is responsible for most of the macrosegregation in castings and ingots. The pressure drop, due to shrinkage and restricted feeding through dendritic structures, is a major factor contributing to the porosity in cast parts. However, experimental measurement of liquid flow in the mushy zone and how it depends upon processing parameters is very difficult. For these reasons, concurrent modeling of segregation and fluid flow is desirable. The microscopic flow of fluid through the mushy zone is usually modeled by Darcy's Law [1]:

$$V = \frac{K}{\mu}\nabla P, \tag{1}$$

where ∇P is the pressure gradient, V is fluid velocity, μ is viscosity and K is the permeability factor. Also, a combined Navier-Stokes (N S) equation, with a Darcy term, is derived by Ganesan and Poirier [2] as follows:

$$\rho_l\left(\frac{\partial \vec{V}}{\partial t} + \vec{V} \quad \nabla\vec{V}\right) = \nabla P + \rho_l \vec{g} + \frac{\mu}{f_l}\nabla^2 \quad f_l \quad \vec{V})$$

$$\mu f_l[K] \quad {}^1\vec{V}, \tag{2}$$

where f_l is liquid fractions, ρ_l is liquid density, $[K]$ is a permeability tensor and K is between zero and infinite, respectively, for solid fractions 1 and 0. When $f_l = 1$ or $f_l = 0$, K will be infinite and zero, respectively. This often proves suitable, if the permeability is known; even if the assumptions used to derive Darcy's law are not entirely satisfied, an effective permeability may give usable results when the length scale under consideration is sufficiently greater than the microstructural length scale. This macroscale effective permeability depends upon the detailed flow pattern at the microscale, which, in turn, depends upon the shape and nature of the channels through which the liquid flows. In the dendritic mushy zone, these shapes are quite complex indeed and both measurement and prediction of the exact flow patterns are difficult. Therefore, a suitable value for the permeability for use in Equation 1 or 2 is often not known. It is well established that growth rate, temperature gradient and composition of material are the main factors that affect dendrite morphology [3,4]. In dendritic alloys, behind the paraboloid tip, secondary arms grow in preferred orientation. Also, as time progresses, tertiary arms may grow and their growth may cease

1. *Department of Mining and Metallurgical Engineering, Amirkabir University of Technology, Tehran, I.R. Iran.*

as they encounter the diffusion field of branches of neighboring dendrites [5,6]. Also, the interdendritic liquid moves in a solid network with a non-uniform volume fraction. In the interior of the mushy zone, where the solid fraction is greater than about one-third, Darcy's law can satisfactorily represent the momentum equation [5]. However, Darcy's law gives erroneous results closer to the liquid zone and it is necessary to use an equation which includes inertial, diffusion and Darcy terms (tensor permeability) [6]. Furthermore, the solid network may not be coherent and, hence, may be moved along with the liquid, resulting in mass feeding [7]. Approaches for estimating permeability include experimental measurement and analytic or numerical solutions of the microscale flow patterns.

In the experimental method, special metallic alloys freeze over a range of temperatures. The solute concentration ahead of the solid/liquid interface leads to a dendritic growth of the solid phase throughout the liquid phase, giving origin to a mushy zone where solid and liquid coexist.

A fine mesh of solid dendrites forms interdendritic channels filled with liquid metal. The tortuousness of the interdendritic channels induces a pressure drop in the liquid flow between the entrance and the bottom of these channels. For typical dendrite arms spacing, the liquid flow in this fine mesh can be treated as a flow through a finely porous media and Darcy's law can be applied to estimate the pressure drop in the channel. Therefore, much research has focused on measuring the permeability of alloys in the mushy zone [8].

Piwonka and Flemings [9] carried out the first measurement of permeability, forcing liquid lead throughout solidifying Al-4.5 wt. Cu%. Later, some other works reported experimental measures of the permeability of alloys under different conditions. Apelian et al. [10] measured the permeability of Al-Si alloys using water as fluid. Streat and Weinberg [11] measured interdendritic flow rate in Pb-20 wt.% Sn alloys using a Pb-Sn alloy as fluid and gravity as the driving force. Nasser-Rafi et al. [12] analyzed the permeability of directionally solidified Pb-20 wt. Sn% alloy, with various primary and secondary dendrite arms spacing, for liquid flow parallel and normal to primary dendrite arms. Using directionally frozen borneol-paraffin organic alloy and an aqueous solution as fluid, Murakami et al. [13,14] carried out some interesting measurements of permeability.

There are two commonly used analytical solutions for calculating non-dimensional permeability for creep flow through periodic or random arrays of cylinders having simple (circular, hexagonal, square) cross-sections. The lubrication model, developed by Bruschke and Advani [15], is applicable for high solid-fraction arrays and the point-particle (dilute) model, developed by Gebart [16], is applicable for low solid fraction arrays. However, so far, analytical approaches are not feasible for more complex shapes approximating real dendrite shapes.

Numerical methods have been used to model actual flow situations simulating dendritic structures [17-23]. These studies have shown that the detailed morphology of the dendrite at microscale has a significant effect on the resistance to flow and, hence, on effective permeability, which may be observed at the macroscale. In spite of the published research, determination of dendritic structural permeability, due to the very complex microstructure of dendrites, still remains a challenge for both mathematical and experimental methods. The detailed microscopic scale models may not yet be feasibly applied to the whole of the mushy zone, consisting of millions of individual dendrite arms. However, a numerical study of the permeability through the simulated microstructures has not so far been approached systematically. To understand the changes in the flow resistance, due to the change of dendrite geometry shape, and how this relates to the material properties and processing parameters, a combination of micro models for solidification and fluid flow has been used. The velocity and pressure from these results are then used to estimate the effective permeability for arrays of dendrite shapes in Al-Si different alloys.

MATHEMATICAL MODELS

Relative motion between the solid and the liquid during alloy solidification is one of the most critical transport phenomena associated with macro segregation and micro structural development. In order to predict the relative movement, as well as its ensuing effects, in a solidifying alloy, accurate knowledge of the solid/liquid interfacial drag and permeability over the entire range of the solid volume fraction is required. Therefore, in the present work, two separate computational models of the grain growth and interdendritic liquid flow are coupled for the modeling of permeability effective in mushy alloys. The grain growth is simulated using a Cellular Automation Finite Difference (CAFD) for a 2D dendrite, and fluid flow by using a Computational Fluid Dynamic (CFD) model for determining effective permeability. The governing equations and details of the numerical solution for each model are given below.

CAFD Model

The CAFD model was used to simulate grain formation [24,25]. The model of the grain growth is based on local thermal and constitutional under cooling [26-29]. The dendritic shapes were simulated assuming an Al-Si binary system with a single nucleation site at the centre of the system domain. The grain morphology

and growth rate are controlled by the partitioning and diffusion phenomena, as described in [29].

Solute Partitioning and Diffusion

Due to the difference between the solubility of solute in the liquid and solid matrix phase, solute partitioning occurs during the solidification process. The solute concentration gradient is the driving force behind the solute diffusion within solid and liquid matrix phases. Assuming local equilibrium, the total concentration of solid solute per cell before eutectic is given by [28,29]:

$$C_S = C_l \left[1 \quad (1 \quad \overline{k}) f_S\right]. \tag{3}$$

Diffusion of Si is calculated using Fick's equation:

$$\frac{\partial}{\partial t}\left[f_S \overline{k} C_l + (1 \quad f_S) C_l\right] = \nabla . D_e \nabla C_l, \tag{4}$$

where the effective diffusion coefficient is $D_e = (1 \quad f_S) D_l + f_S \overline{k} D_S$, $\overline{k}$ is the partition coefficient and C is the solute concentration. This equation was solved using an explicit finite-difference scheme. A weighted average of the solute diffusion coefficient in the liquid and solid phases is applied in partly solid cells [29].

Growth Model

If the solid fraction within a cell is greater than zero, partitioning can occur and the solute is rejected from the cell into its neighboring liquid cells. The solute concentration heterogeneity produced by partitioning drives the diffusion, which tends to harmonize the solute concentration. Partitioning and diffusion, as mentioned above, change the solute concentration and, therefore, the local liquidus temperature via the phase diagram, as well as local undercooling. In each solidifying cell, the change in the solid fraction is firstly determined by the KGT model [26], which calculates the maximum growth rate, based on a given undercooling at a near absolute stability limit. The solid fraction is further corrected by a diffusion-controlled growth. Once the solid fraction reaches a critical value, it can grow into its neighboring liquid cells, providing the cells are under-cooled. When the solid fraction of the cells reaches unity, the cell is considered fully solidified. A liquid cell may be captured by a growing neighboring cell and become part of the solid grain [29,30].

CFD Model

In the present work, a CFD code, SUTCAST, developed to determine 2D permeability by solving the $N \quad S$ equation using the SOLution Algorithm (SOLA) method, which has been described in [31,32] is used. In a solidifying alloy, the interdendritic liquid moves in a solid network, in which the volume fraction of liquid is not uniform. In the interior of the mushy zone, ($0 < f_L < 0.66$), the momentum equation can be satisfactorily represented by Darcy's law. However, in the field of dendritic solidification that gives erroneous results in the part of the mushy zone that is adjacent to the full-liquid zone (where $f_L > 0.66$), it is necessary to use a comprehensive momentum equation with inertial and diffusion terms, along with Darcy's term. Then, for transient flow, $N \quad S$ and continuity equations are [7], as follows:

$$\rho_L \frac{D\vec{V}}{Dt} = \quad \nabla P + \rho_L \vec{g} + \mu \nabla^2 \vec{V}, \tag{5}$$

$$\frac{\rho_L \quad \rho_S}{\rho_m}\left[\frac{\partial f_L}{\partial t} + (\vec{V}).\nabla f_L\right] + \nabla.(\vec{V}) = 0, \tag{6}$$

where f_S and f_L are solid and liquid fractions, respectively, and the density of the mushy zone is $f_S \rho_S + f_L \rho_L = \rho_m$, $f_S + f_L = 1$. It is clear when $f_L < 1$, Equation 6 leads to Equation 2.

The heat transfer equation for the mushy zone may be written as:

$$\rho C_P \frac{\partial T}{\partial t} = \quad \rho C_P \vec{v}.\nabla T + \nabla.\vec{q} + q^{\bullet}, \tag{7}$$

where:

$$q^{\bullet} = \rho \Delta H_m \frac{\partial f_S}{\partial t}, \tag{8}$$

$$\frac{\partial f_S}{\partial t} = \frac{\partial f}{\partial T}\frac{\partial T}{\partial t}. \tag{9}$$

The fraction of solid in the mushy zone is estimated by Equation 10. The CFD program assumes partial mixing in the liquid and no diffusion in the solid phase ($D_S = 0$) [16,17]:

$$C_S = k_E C_L (1 \quad f_S)^{1 \quad k_E}, \tag{10}$$

$$\frac{C_S}{C_L} = \frac{T_m \quad T}{T_e \quad T_L}, \tag{11}$$

where:

$$k_E = \frac{k_{\bullet}}{k_{\bullet} + (1 \quad k_{\bullet}) \exp\left(\frac{\delta R}{D_L}\right)}.$$

Substituting Equation 11 into Equation 10 gives:

$$f_S = 1 \quad \left(\frac{T_m \quad T}{T_e \quad T_L}\right)^{\left(\frac{1}{k_E \quad 1}\right)}, \tag{12}$$

and substituting Equation 12 into Equation 9 gives:

$$\frac{\partial f_S}{\partial t} = \frac{1}{(T_e \quad T_L)(k_E \quad 1)}\left(\frac{T_m \quad T}{T_e \quad T_L}\right)^{\left(\frac{2 \quad k_E}{k_E \quad 1}\right)} \frac{\partial T}{\partial t}. \tag{13}$$

The release of latent heat between the liquidus and solidus temperature is calculated by substituting Equation 13 into Equation 7. Therefore, the heat transfer equation is given by:

$$\rho[C_P'']\frac{\partial T}{\partial t} = \rho C_P \vec{\nu}.\nabla T + \nabla.\vec{q}, \quad (14)$$

where C_P'' can be considered as a quasi-specific heat given by:

$$C_P'' = \left[C_P \ \Delta H_m \frac{1}{(T_e \ T_L)(k_E \ 1)} \left(\frac{T_m \ T}{T_e \ T_L} \right)^{\left(\frac{2 \ k_E}{k_E \ 1}\right)} \right]. \quad (15)$$

To implement this equation in the CFD code, the physical properties of the liquid, solid and mould are assumed constant in the solidification process. However, in the mushy zone, the coefficients of the heat conductivity and the thermal capacity are as $k_M = f_L k_L + f_S k_S$ and $C_p^M = f_L C_P^l + f_S C_P^S$, respectively [33,34].

COMPUTING PROCEDURE

In the present work, two separate codes, the CAFD program for simulation of the grain growth and the CFD program for interdendritic liquid flow, are coupled for modeling of the permeability effective in the mushy alloys. During simulation of the interdendritic fluid flow for a high solid fraction, after solving the $N \quad S$ equations, the local permeability is updated in cells at each time step, using the calculated pressure and velocity fields by adding Darcy's law. The updated permeability is used to determine the new velocity fields and to satisfy the continuity equation in high solid fractions by the iteration procedure. When the continuity equation is satisfied, final permeability will be equal to effective (last iteration) permeability. The computation procedure is as follows:

1. Go to the CAFD code. The calculations made for each time step consist of the following steps:
   (i) Initial settings are determined, including: mesh generation, initiating arrays, the control parameter set up and physical-thermal property parameters;
   (ii) Semi-explicit approximations of Equations 3, 4 and 8 are used to compute the solute concentration and solid fraction;
   (iii) The dimensions (morphology) and properties of dendrite are determined.
2. Go to the CFD code for calculation of the microfluid flow and permeability near the dendrite. The calculations are made for each time step. The basic procedure of advancing a solution through one increment in time, δt, consists of the following steps:
   (i) Semi-explicit approximations of Equations 2 and 5 are used to compute the first guess for new time-level velocities, using the initial conditions or previous time-level values for all advectives, pressures, viscous accelerations and permeability terms;
   (ii) To satisfy the continuity Equation 6, pressure is iteratively adjusted in each cell and the velocity changes, induced by both pressure (δP) and permeability (δK) changes, are added to the velocities computed in the previous iteration. The pressure change for solid fractions $0 \leq f_S \leq 0.6$ and the permeability change for $0.6 < f_S \leq 1.0$ are calculated by Equations 16 and 17, respectively: Where indexes t, b, l and r are top, bottom, right and left, respectively.

$$\delta P_{i,j,k} = D_{i,j,k}\frac{\rho}{\delta t}\left[\frac{1}{\Delta x}\left(\frac{1}{\Delta x_l}+\frac{1}{\Delta x_r}\right) + \frac{1}{\Delta y}\left(\frac{1}{\Delta y_t}+\frac{1}{\Delta y_b}\right)\right]^{1},$$

low solid fractions, (16)

$$\delta K_{i,j,k} = D_{i,j,k}\delta t\left[\left(\frac{1}{\Delta x}\left(\frac{1}{\Delta x_l}+\frac{1}{\Delta x_r}\right) + \frac{1}{\Delta y}\left(\frac{1}{\Delta y_t}+\frac{1}{\Delta y_b}\right)\right)\right]^{1},$$

high solid fractions. (17)

   (iv) Finally, the temperature in each cell is calculated by means of Equation 14.
3. Repeat Step 1 for determining the new dendrite properties and morphology in the new time step.

The flowchart for computing procedures is given in Figure 1 and details of these steps and the iteration procedure are mentioned in Appendix.

COMPARISON TO ANALYTICAL AND SIMULATION MODELS

The CFD code computations were carried out in a square array of cylinders for code validation, as shown in Figure 2. By imposing a flow velocity with low Reynolds numbers in an x direction and periodic boundary conditions at the top and bottom walls of the cell (a quarter cell), the pressure drop across the cell is calculated numerically by solving the full $N \quad S$ equations, using a system domain with dimensions of 1×1 mm and 100×100 square meshes. The

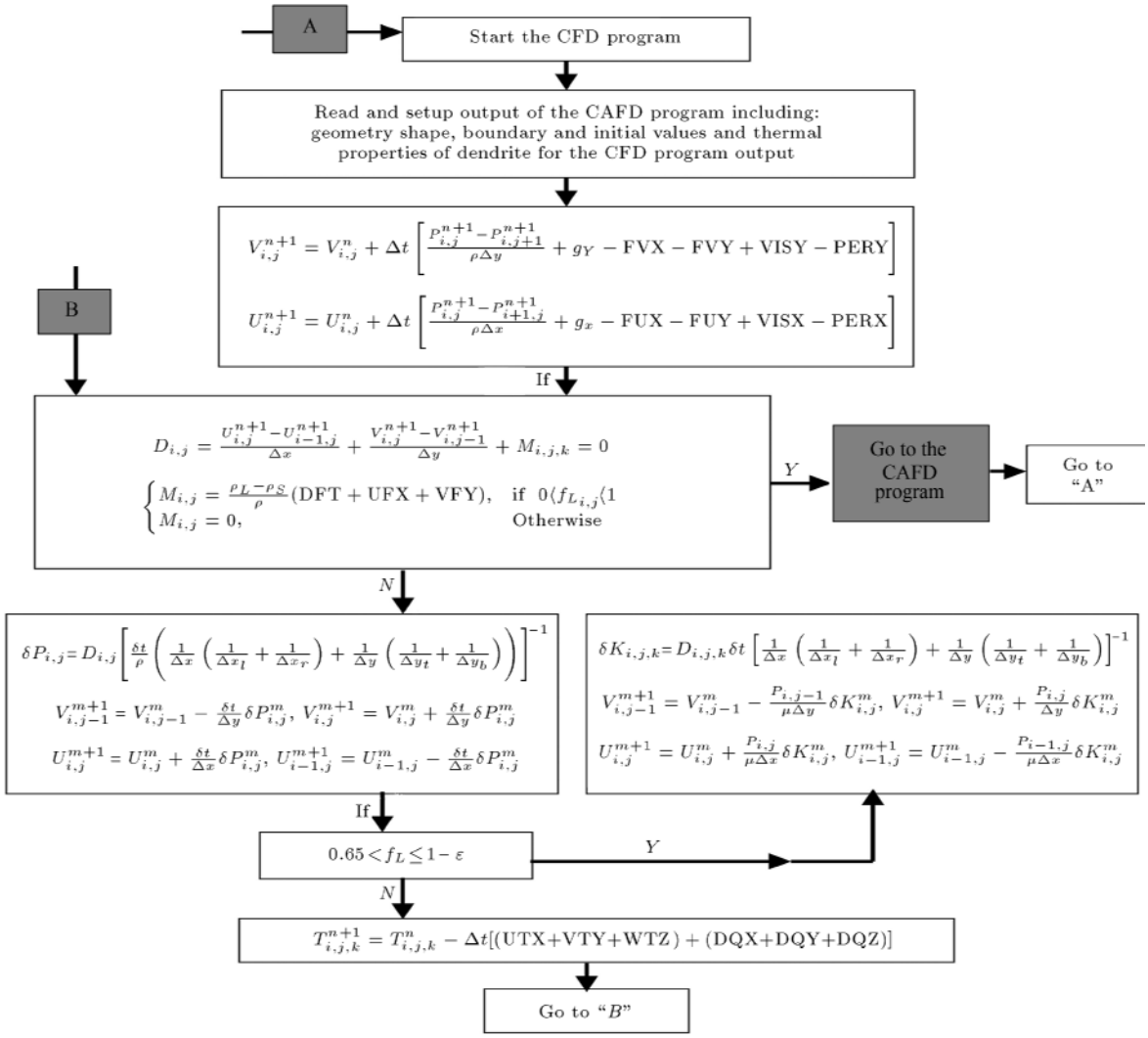

Figure 1. Algorithm of solution $N \quad S$ equations for calculating permeability in low and high solid fractions (all terms are defined in Appendix).

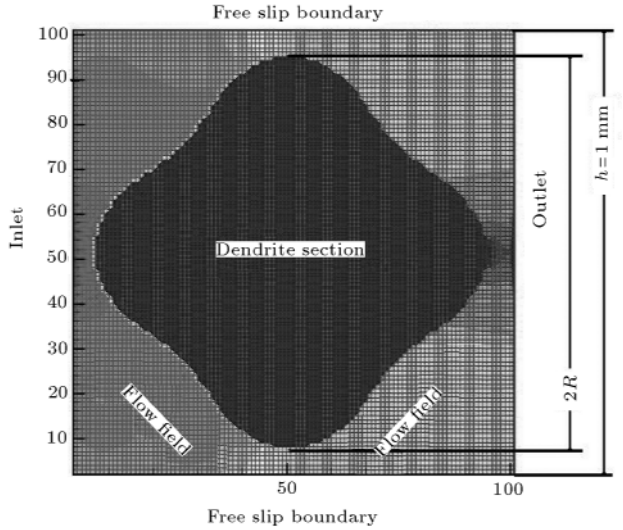

Figure 2. A portion of the unit cell for square array of cylinders.

permeability (k) of the cell is determined from Darcy's law. The effective permeability was normalized by the square of the radius of the cylinder. The developed CFD code was validated by comparing its predication for the effective permeability of the square array of circular cylinders with the asymptotic models of Gebart and Braschke [15,16]. Figure 3 shows the results of the comparison between the CFD code calculated values for normalized permeability and the analytic models for the case of a square array of cylinder for creep flow. The CFD code predictions at high and low porosity are in excellent agreement with the corresponding analytic results of Gebart and Bruschke, respectively.

A FDM solver, Fluent, is used to solve the $N \quad S$ equation for the same conditions as described above. The top and bottom walls of the unit cell were under "no slip" conditions. The left and right walls were "inlet" and "outlet", respectively. Figure 4 shows a comparison of the drag force results between the

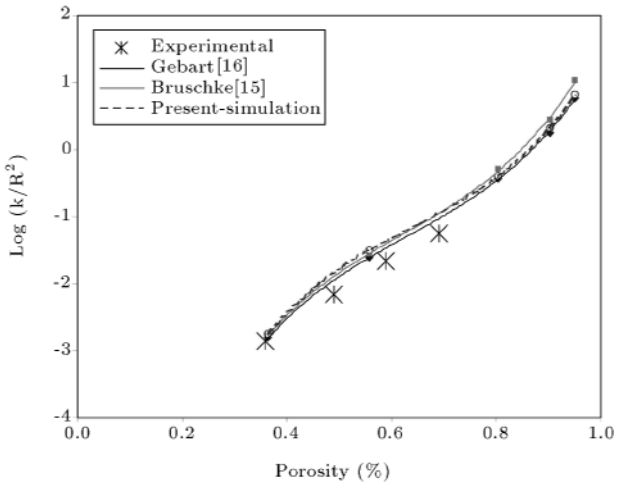

Figure 3. Non-dimension permeability results between the present code (SUT-cast) and analytical solutions [8,9] for validating.

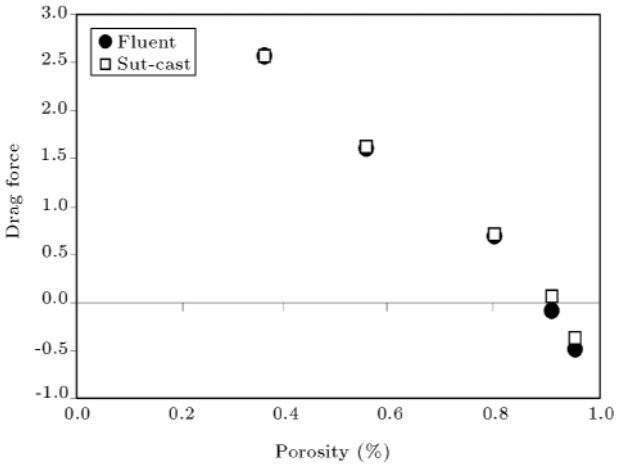

Figure 4. The drag force results between SUT-cast and the fluent code during dendrite growth.

present CFD code and the Fluent code, showing that the present code gives the same results for this case.

RESULTS AND DISCUSSION

In the micro-macro modeling of the columnar solidification of the binary Al-Si alloy, the temperature gradient and growth rate are the main factors that affect the dendrite morphology. The CAFD solver is capable of considering all the factors during solidification. Initially, a nucleus is placed at the centre of a square domain of 1×1 mm. Then, the grain growth program simulates dendritic morphology during solidification, based on the data of Table 1 [33] and growth parameters, such as cooling rate and solute diffusion, at each time step. Then, the fluid flow program simulates the pattern of flow near the dendrites produced by the grain growth program for each separate solid fraction.

Table 1. Physical-thermal data for simulation of Al-Si alloys permeability [33].

	Al-0.1 Si%	**Al-1.0 Si%**	**Al-10 Si%**
k_{sl} **(w/m °k)**	250-190	121-91	81-89
C_P **(J/kg. °k)**	900-990	963-1084	963-1078
T_L **(°C)**	658	644	604
T_S **(°C)**	642	577	577
ρ **(kg/m^3)**	2690-2389	2695-2385	2670-2399
ΔH_m **(kJ/kg)**	396.10	389.2	405.54
μ **(kg/m.sec)**	0.001003	0.001010	0.001098

Finally, permeability is calculated by using Darcy's law, based on the pressure field obtained from the CFD code. Figure 5 shows the iso-pressure fields simulation results obtained around the dendrites of Al-Si alloys. As observed, with increasing Si, the section-area of the columnar dendrites changes from a rhombic toward a cloverleaf morphology, which affects the flow pattern and pressure field of the interdendritic liquid.

Figure 6 shows that the permeability logarithm varies with Si concentration in the ranges (0.414-0.423) of the solid fractions. As shown, an increase in Si percentage leads to a decrease in permeability. The permeability reduction is due to the evolution of the dendrite morphology from a rhombic toward a cloverleaf shape, as shown in Figure 5. As mentioned in the introduction, drag force and permeability are strongly dependent on the orientation of the pressure gradient, with respect to the axes of the growth dendrite. For this reason, the influence of the dendrite rotation angle, with respect to the flow direction, on permeability, was simulated. Figure 7 shows the permeability simulation results for a dendrite with a cloverleaf cross-section and a fixed Si percentage. As observed, an increase in permeability increases the rotation angle until 45 degrees, because the distance between the cell wall and the tip of the dendrite has increased. This effect is dependent on symmetry, arm number, shape and perturbation of the dendrite. For example, the rotation angle for a dendrite with a circle section (zero perturbation) will not have any effect on the permeability. Figure 8 shows both the effect of Si concentration and dendrite rotation for a fixed solid fraction. From Figure 8 it can be concluded that in a solid fraction and fixed angle, there are different values of permeability, which expresses the magnitude of the effect on dendrite shape.

CONCLUSION

1. In this investigation an algorithm was developed to calculate the permeability of mushy alloys for low and high solid fractions. To simulate permeability, both the CFD and the CAFD codes were coupled.

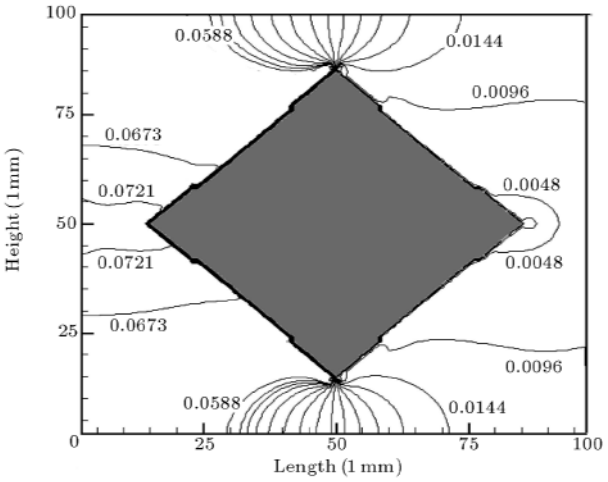

(a) Si=0.1%

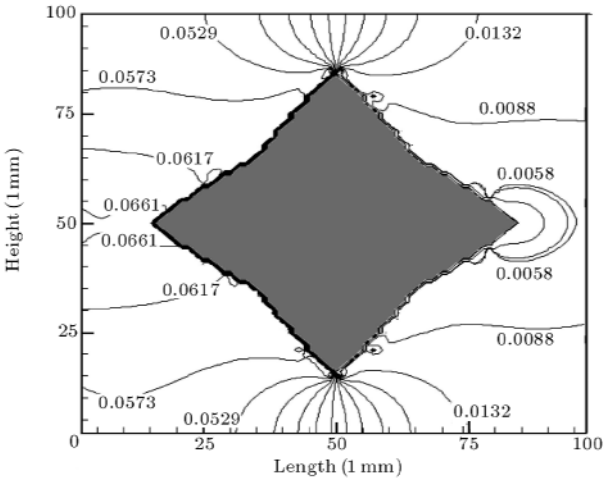

(b) Si=1.0%

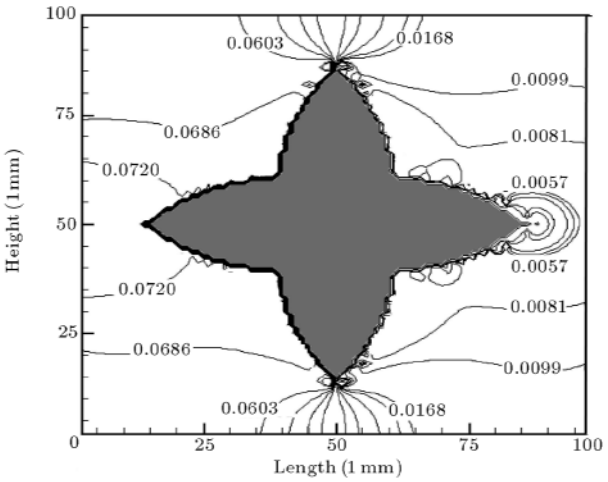

(c) Si=10.0%

Figure 5. Iso-pressure (Pa) contours for flow parallel to the axis of symmetry of a square cell in the Al-wt. Si% alloys with solid fraction 0.24 and the length $h = 1$ mm at Re = 0.1 with 100×100 elements.

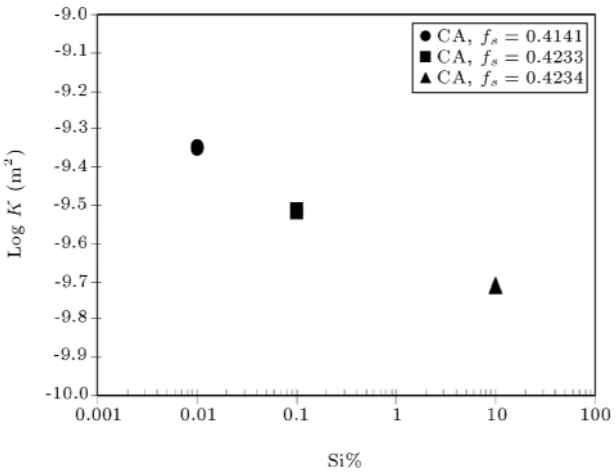

Figure 6. Effect of Si concentration on permeability during dendrite growth. CA: Cellular automation code.

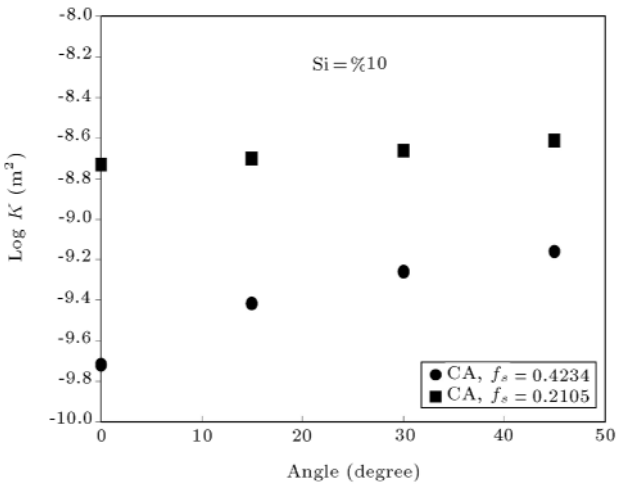

Figure 7. Effect of angle between dendrite arm and streamline on permeability in a fixed Si% during dendrite growth.

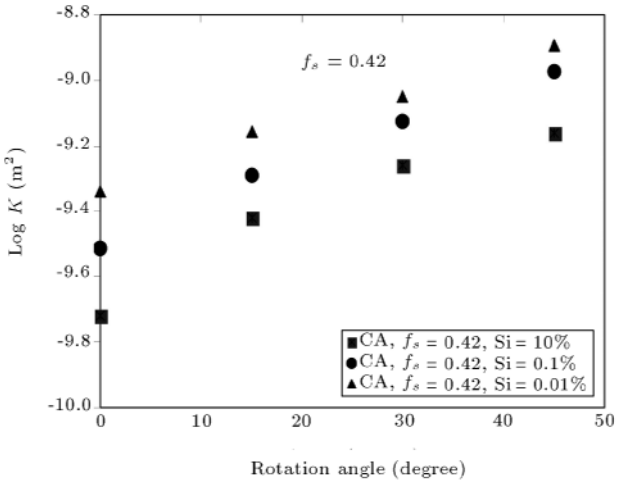

Figure 8. Effect of angle between dendrite arm and streamline on the permeability in a fixed solid fraction.

The CAFD created dendrite and the CFD calculated fluid flow near the dendrite;

2. Comparisons between the calculated permeability and experimental data extracted from different authors, permit one to conclude that the present model, based on Equations 16 and 17, describes satisfactorily the variation of permeability with high solid fractions and dendrite morphology in Al-Si% alloys;
3. Simulation results show that solute concentration can convert dendrite morphology from rhombic toward cloverleaf. These concentration variations are in a power-law form. Consequently, the cloverleaf dendrite morphology could decrease the permeability and pattern flow, due to an increase in its drag force;
4. Results of simulation show that in a fixed solid fraction, flow pattern and permeability could alter the dendrite shape and angle between the dendrite axes with streamline.

ACKNOWLEDGMENT

The authors are grateful for the research support of Sharif University of Technology and the Department of Materials at Imperial College, London.

REFERENCES

1. Darcy. H., *Les Fontaines Publiques De Ville de Dijon* (1856).
2. Ganesan, S. and Poirier, D.R. "Conversation of mass and momentum for the flow of interdendritic during solidification", *Metallurgical and Materials Transactions*, **21B**, p 173 (1990).
3. Wang, C.Y., Ahuja, S. and Beckermana, C. "Multiparticle interfacial drag in equiaxed solidification", *Metallurgical and Materials Transactions*, **26**, p 111 (1995).
4. De Groh, H.C.I., Weidman, P.D., Zakhem, R., Ahuja, S. and Beckermann, C. "Calculation of dendrite settling velocities using a porous envelope", *Metallurgical Transactions B-Process Metallurgy*, **240**, p 749 (1993).
5. Brown, S.G.R., Spittle, J.A. and Walden-Bevan, R. "Numerical determination of liquid flow permeabilities for equiaxed dendritic structures", *Acta. Materialia*, **50**, p 1559 (2002).
6. Ganesan, S. and Chan, C.L. "Permeability for flow parallel to primary dendrite arms", *Materials Science and Engineering*, **151**, p 97 (1992).
7. Bahat, M.S., Poirier, D.R. and Heinrich, J.C. "Permeability for cross flow through columnar dendritic alloys", *Metallurgical and Materials Transactions*, **26**, p 1049 (1995).
8. Duncan, A.J., Han, Q. and Viswanathn, S. "Permeability for flow of liquid through equiaxial mushy zones", *Metallurgical and Materials Transactions*, **30B**, p 745 (1999).
9. Piwonka, T.S. and Flemings, M.C. "Pore formation in solidification", *Trans. Metall. Soc.*, **AIME 236**, pp 1157-1165 (1966).
10. Apelian, D., Flemings, M.C. and Mehrabian, R. "Specific permeability of partially solidified dendritic networks of Al-Si alloys", *Metall. Trans.*, **5**, pp 2533-2537 (1974).
11. Streat, N. and Weinberg, F. "Interdendritic fluid in a lead-tin alloy", *Metall. Trans.*, **B7**, pp 417-423 (1976).
12. Nielsen, O. et al. "Measurements and modeling of the micro structural morphology during equiaxed solidification of Al-Cu alloys", *Metall. Trans.*, **A 32**, pp 2049-2060 (2001).
13. Liu, C.Y., Murakami, K. and Okamoto, T. "Modeling the effect of capillary pressure on a liquid flow in a porous medium", *Acta. Metall.* **34**, pp 1173-1178 (1986).
14. Murakami, K., Shiraishi, T. and Okamoto, T. "Fluid flow in interdendritic space in cubic alloys", *Acta. Metall.*, **32**, pp 1423-1428 (1984).
15. Bruschke, M.V. and Advani, S.G. "Flow of generalized newtonian fluids across a periodic array of cylinders", *Journal Rheology*, **37**, p 479 (1993).
16. Gebart, B.R. "Permeability of unidirectional reinforcements for RTM", *Journal Composite Materials*, **26**, p 1100 (1992).
17. McCartney, J.F. "Flow through arrays of cylinder: Lattice gas cellular automate simulations", *Phys. Fluids*, **6**, p 435 (1994).
18. Donald, L. and Koch, C. "Moderate Reynolds number flows through periodic and random arrays of aligned cylinders", *J. Fluid Mech.*, **349**, p 31 (1997).
19. Edwards, D.A. and Shapiro, M. "The influence of Reynolds number upon the apparent permeability of spatially periodic arrays of cylinders", *Phys. Fluid*, **2**, p 45 (1990).
20. Ghaddar, C.K. "Modeling fluid flow near equiaxed dendrites", *Phys. Fluids*, **7**, p 2563 (1995).
21. Nagelhout, D. and Bhat, M.S. "Permeability for flow normal to a sparse array of fibres", *Mate. Sci. Eng.*, **191**, p 203 (1995).
22. Bernard, D., Nielsen, O., Salvo, L. et al. "Permeability assessment by 3D interdendritic flow simulations on microtomography mappings of Al-Cu alloys", *Metall. Trans.*, **A 392**(1-2), pp 112-120 (2005).
23. Eidsath, A. "Dispersion in pulsed systems-III: Comparison between theory and experiments for packed beds", *Chemical Engineering Science*, **38**, p 1803 (1983).
24. Atwood, R.C., Sridhar, S., Zhang, W. and Lee, P.D. "Diffusion-controlled growth of hydrogen pores in aluminium-silicon castings: In situ observation and modeling", *Acta Materialia*, **48**(2), pp 405-417 (2000).

25. Lee, P.D., Chirazi, A. and See, D. "Modeling microporosity in aluminium-silicon alloy", *Journal of Light Metals*, **1**, p 15 (2001).

26. Kurz, W., Giovanola, B. and Trivedi, R. "Theory of microstructural development during rapid solidification", *Acta. Metallurgica*, **34**, p 823 (1986).

27. Kurz, W. and Bezencon, C. "Columnar to equiaxed transition in solidification processing", *Science Technology and Advance Materials*, **12**, p 185 (2001).

28. Kailasam, S.K. and Glicksman, M.E. "A simplified method for calculating the diffusivity matrix in ternary alloys", *Acta. Materialia*, **34**, p 823 (1986).

29. Lee, P.D., Atwood, R.C., Dashwood, R.J. and Nagaumi, H. *Materials Science and Engineering*, **A 328**(1-2), pp 213-222 (2000).

30. Dong, H.B. and Lee, P.D. "Modeling of porosity formation in direct chill cast aluminium-magnesium alloys", *Acta. Materialia*, **53**, pp 659-668 (2005).

31. Mirbagheri, S.M.H., Varahram, N. and Davami, P. "3D computer simulation of melt flow and heat transfer in the lost foam casting process", *Int. Journal for Num. Methods in Engineering*, **58**, p 723 (2003)

32. Hirt, C.W. and Nichols, B.D., *Journal Computational Physics*, **39**, p 201 (1981).

33. Peres, M.D., Siqueira, C.A. and Garcia, A. "Macro structural and micro structural development in Al-Si alloys directionally solidified under unsteady-state conditions", *Journal of Alloys and Compounds*, **381**(1-2), pp 168-181 (2004).

34. Santos, R.G. and Melo, M.L.N.M. "Permeability of interdendritic channels", *Materials Science and Engineering*, **A 391**(1-2), pp 151-158 (2005).

APPENDIX

Finite Difference Approximations

1. The finite difference approximations of the momentum transport equation are [31]:

$$U_{i,j}^{n+1} = U_{i,j}^{n} + \Delta t \left[\frac{P_{i,j}^{n+1} \quad P_{i+1,j}^{n+1}}{\rho \Delta x} + g_x \quad \text{FUX} \right.$$
$$\left. \text{FUY} + \text{VISX} \quad \text{PERX} \right], \qquad \text{(A1)}$$

$$V_{i,j}^{n+1} = V_{i,j}^{n} + \Delta t \left[\frac{P_{i,j}^{n+1} \quad P_{i,j+1}^{n+1}}{\rho \Delta y} + g_Y \quad \text{FVX} \right.$$
$$\left. \text{FVY} + \text{VISY} \quad \text{PERY} \right], \qquad \text{(A2)}$$

$$\text{FUX} = \frac{U_{i,j}^{n}}{2\Delta x}[\text{DUL} + \text{DUR} + \alpha \ \text{Sign}(U_\alpha)(\text{DUL} \quad \text{DUR})],$$

$$\text{PERX} = \frac{U_{i,j}^{n}}{K_{i,j}} \mu f_{i,j} [\text{DUL} + \text{DUR} + \alpha \ \text{Sign}(U_\alpha)(\text{DUL} \quad \text{DUR})],$$

$$\text{VISX} = \upsilon \left(\frac{U_{i+1,j}^{n} \quad 2U_{i,j}^{n} + U_{i \ 1,j}^{n}}{\Delta x^2} + \frac{U_{i,j+1}^{n} \quad 2U_{i,j}^{n} + U_{i,j \ 1}^{n}}{\Delta y^2} \right),$$

$$\text{DUL} = U_{i,j}^{n} \quad U_{i \ 1,j}^{n},$$

$$\text{DUR} = U_{i+1,j}^{n} \quad U_{i,j}^{n},$$

$$U_\alpha = (\text{DUR} + \text{DUL})/2,$$

where the superscript (n) stands for old time level and $(n+l)$ for the new time level. $\alpha = 0$ or 1 is the control factor for upwind and centered differencing, respectively. A similar method is used for calculation of the advective flux terms, FUY, FVX, FVY, the viscous flux term, VISY, and the permeability term, PERY;

2. The finite difference approximation to the continuity equation is:

$$D_{i,j} = \frac{U_{i,j}^{n+1} \quad U_{i \ 1,j}^{n+1}}{\Delta x} + \frac{V_{i,j}^{n+1} \quad V_{i,j \ 1}^{n+1}}{\Delta y} + M_{i,j,k} = 0, \qquad \text{(A3)}$$

$$\begin{cases} M_{i,j} = \frac{\rho_L \ \rho_S}{\rho} (\text{DFT} + \text{UFX} + \text{VFY}) & \text{if } 0 \langle f_{L_{i,j}} \langle 1 \\ M_{i,j} = 0 & \text{Otherwise} \end{cases},$$

$$\text{DFT} = \frac{f_{L_{i,j}}^{n+1} \quad f_{L_{i,j}}^{n}}{\Delta t},$$

$$\text{VFY} = 0.5 \left(V_{i,j} + V_{i,j \ 1} \right) \frac{f_{L_{i,j+1}}^{n} \quad f_{L_{i,j \ 1}}}{2\Delta y},$$

$$\text{UFX} = 0.5 \left(U_{i,j} + U_{i \ 1,j} \right) \frac{f_{L_{i+1,j}}^{n} \quad f_{L_{i \ 1,j}}^{n}}{2\Delta x}. \qquad \text{(A4)}$$

3. The finite difference approximation of the heat transfer equation is:

$$T_{i,j}^{n+1} = T_{i,j}^{n} \quad \Delta t\{(\mathrm{UTX} + \mathrm{VTY}) + (\mathrm{DQX} + \mathrm{DQY})\}, \tag{A5}$$

$$\mathrm{UTX} = 0.5\Big\{(1+\alpha)U_{i\ \ 1,j}(\mathrm{DTXL}) + (1 \quad \alpha)U_{i,j}(\mathrm{DTXR})\Big\},$$

$$\mathrm{DTXL} = \frac{T_{i,j} \quad T_{i\ \ 1,j}}{\Delta x},$$

$$\mathrm{DTXR} = \frac{T_{i+1,j} \quad T_{i,j}}{\Delta x},$$

$$\mathrm{DQX} = \frac{QXR \quad QXL}{\rho C_P \Delta x}.$$

The VTY is found in a similar way to UTX. If cells (i,j) and $(i+1,j)$ are liquid cells, then:

$$\mathrm{QXR} = \quad k_R \frac{T_{i+1,j}^{n} \quad T_{i,j}^{n}}{\Delta x},$$

$$\mathrm{QXL} = \quad k_l \frac{T_{i,j}^{n} \quad T_{i\ \ 1,j}^{n}}{\Delta x}.$$

DQY is found in a similar way. In the freezing range, the specific heat and liquid in the new time step $(n+1)$ in the CFD program, the first guess for the new time level, namely, U^{n+1}, V^{n+1} and W^{n+1} are calculated by an explicit approximation with the old time-level (n) values. In the first step of the solution, therefore, the P^{n+1} values in Equations A1 and A2 are replaced by P^{n}. Then, the guessed velocities are put into the continuity Equation A3. In order to satisfy the continuity Equation A3, the velocities, as well as the pressures, should be adjusted iteratively with Equations 16 and 17 for the computational cells with low and high solid fractions, respectively.

For cells of low solid fractions $(0 \le f_S \le 0.6)$ in each iteration, with $\delta P_{i,j}$ determined, new estimates for $P_{i,j}$ and the velocities on the sides of the cell are found, as follows:

$$P_{i,j}^{m+1} = P_{i,j}^{m} + \delta P_{i,j}^{m},$$

$$\delta P_{i,j} = D_{i,j}\left[\frac{\delta t}{\rho}\left(\frac{1}{\Delta x}\left(\frac{1}{\Delta x_l} + \frac{1}{\Delta x_r}\right) + \frac{1}{\Delta y}\left(\frac{1}{\Delta y_t} + \frac{1}{\Delta y_b}\right)\right)\right]^{1}, \tag{A6}$$

$$U_{i,j}^{m+1} = U_{i,j}^{m} + \frac{\delta t}{\Delta x}\delta P_{i,j}^{m},$$

$$U_{i\ \ 1,j}^{m+1} = U_{i\ \ 1,j}^{m} \quad \frac{\delta t}{\Delta x}\delta P_{i,j}^{m}, \tag{A7}$$

$$V_{i,j}^{m+1} = V_{i,j}^{m} + \frac{\delta t}{\Delta y}\delta P_{i,j}^{m},$$

$$V_{i,j\ \ 1}^{m+1} = V_{i,j\ \ 1}^{m} \quad \frac{\delta t}{\Delta y}\delta P_{i,j\ \ 1}^{m}. \tag{A8}$$

For cells of high solid fractions $(0.6 < f_S \le 1.0)$ in each iteration, with $K_{i,j}$ determined, new estimates for the velocities on the sides of the cell are found as follows:

$$K_{i,j}^{m+1} = K_{i,j}^{m} + \delta K_{i,j}^{m},$$

$$\delta K_{i,j,k} = D_{i,j,k}\delta t\left[\left(\frac{1}{\Delta x}\left(\frac{1}{\Delta x_l} + \frac{1}{\Delta x_r}\right) + \frac{1}{\Delta y}\left(\frac{1}{\Delta y_t} + \frac{1}{\Delta y_b}\right)\right)\right]^{1}, \tag{A9}$$

$$V_{i,j\ \ 1}^{m+1} = V_{i,j\ \ 1}^{m} \quad \frac{P_{i,j\ \ 1}}{\mu\Delta y}\delta K_{i,j}^{m},$$

$$V_{i,j}^{m+1} = V_{i,j}^{m} + \frac{P_{i,j}}{\Delta y}\delta K_{i,j}^{m}, \tag{A10}$$

$$U_{i,j}^{m+1} = U_{i,j}^{m} + \frac{P_{i,j}}{\mu\Delta x}\delta K_{i,j}^{m},$$

$$U_{i\ \ 1,j}^{m+1} = U_{i\ \ 1,j}^{m} \quad \frac{P_{i\ \ 1,j}}{\mu\Delta x}\delta K_{i,j}^{m}. \tag{A11}$$

The above velocities are then put into the continuity equation again and the outlined procedures are repeated. Convergence of iteration is achieved when all cells have $D_{i,j}$ values satisfying the inequality, $D_{i,j} < \varepsilon$, as shown in the flowchart of Figure 1.